Available online at www.sciencedirect.com
ScienceDirect
International Journal of Solids and Structures 44 (2007) 8579–8599
INTERNATIONAL JOURNAL OF SOLIDS AND STRUCTURES
www.elsevier.com/locate/ijsolstr

Stress intensity factors for three-dimensional cracks in functionally graded materials using enriched finite elements

Ali O. Ayhan *

GE Global Research Center, One Research Circle, Niskayuna, NY 12309, USA

Received 7 April 2007; received in revised form 19 June 2007; accepted 25 June 2007
Available online 29 June 2007

Abstract

A three-dimensional enriched finite-element methodology is presented to compute stress intensity factors for three-dimensional cracks contained in functionally graded materials (FGMs). A general-purpose 3D finite-element based fracture analysis program, FRAC3D, is enhanced to include this capability. First, using available solutions from the literature, comparisons have been made in terms of stresses under different loading conditions, such as uniform tensile, bending and thermal loads. Mesh refinement studies are also performed. The fracture solutions are obtained for edge cracks in an FGM strip and surface cracks in a finite-thickness FGM plate and compared with existing solutions in the literature. Further analyses are performed to study the behavior of stress intensity factor near the free surface where crack front terminates. It is shown that three-dimensional enriched finite elements provide accurate and efficient fracture solutions for three-dimensional cracks contained in functionally graded materials.

Keywords: Enriched finite elements; Functionally graded materials; Surface cracks; Stress intensity factor; Free-surface effects

1. Introduction

The materials development and engineering analyses of functionally graded materials (FGMs) have been a widespread and active effort in the last two decades in the materials and engineering mechanics research communities. Originally, the concept of functionally graded materials was proposed as an alternative to thermal barrier coatings (TBCs), which are used in aerospace and high temperature applications, to overcome their well-documented shortcomings (Erdogan, 1995). Some of these shortcomings are low toughness, brittleness and poor interfacial bonding resulting in spallation. FGMs are multi-phase materials in which the volume fractions of the constituents vary as a function of position, typically in the thickness direction. For example, the material composition may be such that it contains 100% metal at the interface and 100% ceramic at the coating surface. Therefore, the mismatch of thermo-mechanical properties near the bond line is minimized, while high temperature, wear and oxidation resistance are still achieved on the exposed surface of the

* Tel.: +1 518 387 5742; fax: +1 518 387 7006.
E-mail address: Ayhan@ge.com

0020-7683/$ - see front matter
doi:10.1016/j.ijsolstr.2007.06.022

FGM coating. Another application area of FGMs is in the area of composite materials where they can act as a transition zone between two different layers bonded together. This is achieved by placing a transitional zone between the bonded layers such that its material properties vary to match those of both materials from one interface to the other. This also, through minimization of material property mismatches near the bond lines, allows reduction in residual stresses and interfacial delamination (Lee and Erdogan, 1995).

The research and advancements in functionally graded material development and manufacturing also require the support of engineering mechanics and analysis. In this regard and specifically in the area of fracture mechanics, there has been extensive research focusing on predicting response of FGM structures containing cracks. Initial efforts on analytical studies of cracks in FGMs were on the asymptotic stress fields near the crack tip. Delale and Erdogan (1983) studied the mode-I crack problem in a nonhomogeneous infinite plane and showed that the square root stress singularity is conserved and that the effect of the Poisson's ratio on stress intensity factors (K) is negligible. Eischen (1987) also studied the crack tip stress fields by using eigenfunction technique and showed that the angular functions associated with the first two terms ($r^{-1/2}$ and r^0) in the asymptotic stress field for a crack in an FGM are the same as those in the well-known field for homogeneous materials (Williams, 1957). Konda and Erdogan (1994) solved the mixed-mode crack problem in FGMs. Erdogan and Wu (1997) studied the edge crack problem for a finite-thickness strip and provided fracture solutions for uniform tensile, bending and grip loads. Anlas et al. (2002) studied the extent and the shape of the K-dominant zone in continuously nonhomogeneous materials by comparing the analytically known stress fields to stresses obtained from a full-field finite-element solution. Dolbow and Gosz (2002) used the interaction energy integral to compute mixed-mode stress intensity factors for two-dimensional cracks in FGMs. Parameswaran and Shukla (2002) studied the asymptotic stress field for stationary cracks aligned along the direction of property variation in an FGM with exponentially varying elastic modulus. They obtained the first six terms of the expansion for opening and shear modes of crack deformation. More recent experimental fracture mechanics studies can also be found in the literature (Butcher et al., 1998; Parameswaran and Shukla, 1998; Carpenter et al., 2000; Abanto-Bueno and Lambros, 2002).

Although initially most analytical and numerical fracture mechanics studies in FGMs focused on two-dimensional plane problems, more recently solutions for three-dimensional cracks have also been reported in the literature. For example, Walters et al. (2004) employed the J-integral (Rice, 1968) using a domain integral approach to obtain fracture solutions for semi-elliptical surface cracks contained in FGM structures. Using the displacement correlation technique, Yildirim et al. (2005) studied the behavior of a semi-elliptical surface crack in an FGM coating bonded to a homogeneous substrate under mechanical or transient thermal loading conditions. Recently, Walters et al. (2006) also reported mixed-mode stress intensity factors for three-dimensional cracks in FGMs using a two-state interaction integral method.

In this study, enriched finite elements are used to compute stress intensity factors for three-dimensional cracks contained in FGMs. A general-purpose finite-element program, FRAC3D (Ayhan and Nied, 1999), is enhanced to include this capability. First, stress analyses are performed and comparisons are made for some cases available in the literature considering different types of loading. Then, results from three-dimensional fracture analyses are presented for edge and surface cracks and comparisons are made to the solutions available in the literature. It is demonstrated that enriched elements are suitable to accurately compute fracture parameters for three-dimensional cracks in FGMs in a straightforward and efficient manner without the need for special finite element meshes and post-processing of the results. In the following sections, the finite-element formulation implemented in FRAC3D and numerical examples are presented.

2. Finite-element formulation

In this section, details of the finite-element formulation for stress and fracture analyses of FGMs are presented. Similar to many other studies in the literature, the form of the material property gradient functions is selected to be exponential. For example, for the finite-thickness strip shown in Fig. 1, the elastic modulus and coefficient of thermal expansion (CTE) vary according to

$$E(x) = E_1 e^{\beta x} \quad \text{and} \quad \alpha(x) = \alpha_1 e^{wx}, \tag{1}$$

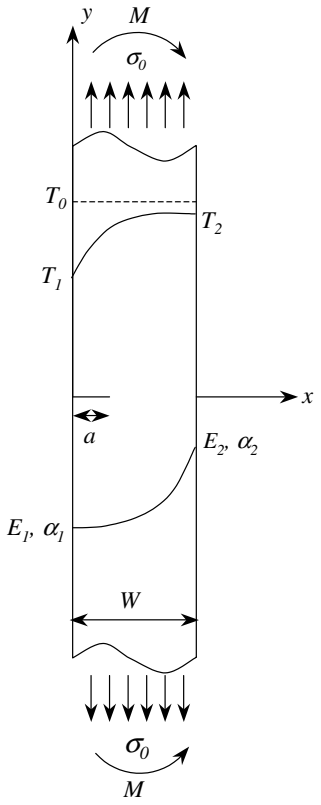

Fig. 1. A functionally graded semi-infinite strip containing an edge crack.

where

$$\beta = \frac{1}{W}\ln\left(\frac{E_2}{E_1}\right) \quad \text{and} \quad w = \frac{1}{W}\ln\left(\frac{\alpha_2}{\alpha_1}\right). \tag{2}$$

E_1, α_1, and E_2, α_2 are the values of elastic modulus and CTE at $x = 0$ and $x = W$, respectively.

2.1. Stress analysis

A general-purpose finite-element code can easily be modified to account for spatial variations in material properties of FGMs. Walters et al. (2004) describe different ways of incorporating this into a finite-element program. These include using constant material property for each element in the model based on its location in the structure and prescribing temperature dependent material properties combined with a corresponding temperature field imposed on the finite-element model such that when accounted for, the desired spatial material property variation is achieved. Another way is to compute material properties at each integration point during element stiffness matrix formation by calculating its coordinate and the corresponding material properties via the property variation functions, e.g., Eq. (1). In this study, material properties are computed at each integration point for element stiffness matrix and the corresponding force vector to account for contributions from thermal loads involving spatially varying CTE.

The stiffness matrix for a given finite element is obtained by Cook et al. (1989)

$$[k] = \int_{-1}^{1}\int_{-1}^{1}\int_{-1}^{1}[B]^{\mathrm{T}}[E][B]\boldsymbol{J}\,\mathrm{d}\xi\,\mathrm{d}\eta\,\mathrm{d}\rho. \tag{3}$$

In the case of functionally graded material, the elasticity matrix, $[E]$, is a function of position and can take different values for different integration points used in the Gaussian quadrature,

$$[k] = \sum_{i=1}^{nint} \sum_{j=1}^{nint} \sum_{k=1}^{nint} W_i W_j W_k \phi(\xi_i, \eta_j, \rho_k) \boldsymbol{J}, \tag{4}$$

where Wi's are the weights at the sampling Gauss points, ξ_i, η_j, ρ_k, and $\phi(\xi_i, \eta_j, \rho_k)$ is a 60 by 60 matrix for a 20-noded quadratic hexahedron element, obtained from evaluation of the matrices in the integrand, $[B]^{\mathrm{T}}[E][B]$, and $\boldsymbol{J}$ is the determinant of the Jacobian matrix.

Similarly, in the case of thermal loading, the gradients in material properties can be taken into account in the right-hand side or element force vector (Cook et al., 1989);

$$\{r_e\} = \int_{V_e} [B]^{\mathrm{T}}[E]\{\varepsilon^0\}\mathrm{d}V - \int_{V_e} [B]^{\mathrm{T}}\{\sigma^0\}\mathrm{d}V + \int_{V_e} \{N\}^{\mathrm{T}}\{\mathrm{F}\}\mathrm{d}V + \int_{S_e} \{N\}^{\mathrm{T}}\{\Phi\}\mathrm{d}S. \tag{5}$$

The first volume integral in Eq. (5) accounts for elemental consistent nodal forces due to thermal loading and takes the following form

$$\{r_e\} = \int_{-1}^{1}\int_{-1}^{1}\int_{-1}^{1} [B]^{\mathrm{T}}[E] \begin{Bmatrix} \alpha_x \Delta T(\xi,\eta,\rho) \\ \alpha_y \Delta T(\xi,\eta,\rho) \\ \alpha_z \Delta T(\xi,\eta,\rho) \\ \alpha_{xy} \Delta T(\xi,\eta,\rho) \\ \alpha_{yz} \Delta T(\xi,\eta,\rho) \\ \alpha_{xz} \Delta T(\xi,\eta,\rho) \end{Bmatrix} \boldsymbol{J}\,\mathrm{d}\xi\,\mathrm{d}\eta\,\mathrm{d}\rho. \tag{6}$$

As can be seen from Eq. (6), both elasticity matrix and the thermal strain vector can be functions of position when both of these material properties are graded. Taking this into account, Eq. (6) is also integrated using Gaussian quadrature similar to Eq. (4). The remaining integral terms, in their respective order, in Eq. (5) are for consistent nodal forces due to initial stress, concentrated forces acting within the element volume and distributed forces acting on the element surfaces.

2.2. Fracture analysis

In this section, the formulation of enriched crack tip elements for three-dimensional crack problems in FGMs is presented. Consider an enriched finite element located at the crack tip (Fig. 2). The displacements for this element are given by

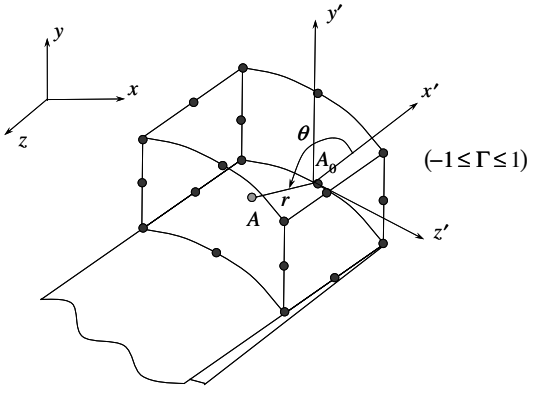

Fig. 2. Schematic of a 20-noded enriched finite element located at portion of an arbitrarily oriented crack.

$$u(\xi,\eta,\rho)=\sum_{j=1}^{r}N_j(\xi,\eta,\rho)u_j+Z_0(\xi,\eta,\rho)\{K_{\mathrm{I}}(\Gamma)F_1(\xi,\eta,\rho)+K_{\mathrm{II}}(\Gamma)G_1(\xi,\eta,\rho)+K_{\mathrm{III}}(\Gamma)H_1(\xi,\eta,\rho)\},\quad(7)$$

$$v(\xi,\eta,\rho)=\sum_{j=1}^{r}N_j(\xi,\eta,\rho)v_j+Z_0(\xi,\eta,\rho)\{K_{\mathrm{I}}(\Gamma)F_2(\xi,\eta,\rho)+K_{\mathrm{II}}(\Gamma)G_2(\xi,\eta,\rho)+K_{\mathrm{III}}(\Gamma)H_2(\xi,\eta,\rho)\},\quad(8)$$

$$w(\xi,\eta,\rho)=\sum_{j=1}^{r}N_j(\xi,\eta,\rho)w_j+Z_0(\xi,\eta,\rho)\{K_{\mathrm{I}}(\Gamma)F_3(\xi,\eta,\rho)+K_{\mathrm{II}}(\Gamma)G_3(\xi,\eta,\rho)+K_{\mathrm{III}}(\Gamma)H_3(\xi,\eta,\rho)\}.\quad(9)$$

In (7)–(9) u_j, v_j and w_j represent the r unknown nodal displacements and $N_j(\xi,\eta,\rho)$ are the conventional element shape functions in terms of the element's local coordinates. $K_{\mathrm{I}}(\Gamma)$, $K_{\mathrm{II}}(\Gamma)$, $K_{\mathrm{III}}(\Gamma)$ represent the mode-I, -II and -III stress intensity factors varying along the crack front and are defined by the unknown nodal stress intensity factors, K_{I}^i, K_{II}^i, K_{III}^i, and element shape functions $N_i(\Gamma)$ evaluated along the edge located on the crack front. Although all three modes of stress intensity factors can be computed using the three-dimensional enriched elements (Ayhan, 2004, 2007), focus in this study is given to mode-I fracture in FGMs. Z_0 is a linear transition function for the elements that surround the crack tip elements and take a value of "1" at surfaces shared with crack tip elements including everywhere in the enriched element, and "0" on faces that are shared with the regular finite elements (Ayhan, 1999; Ayhan and Nied, 2002). For a quadratic hexahedral enriched element, in addition to the 60 unknown nodal displacements, a total of nine (three for each mode) unknown stress intensity factors are also included in the element formulation. As a result, the unknown nodal displacements and stress intensity factors are solved simultaneously during solution of the system of finite-element equations. Unlike some other methods such as displacement correlation and J-integral, enriched finite-element method eliminates the need for post-processing the finite-element solution to obtain the fracture parameters.

The functions F_i, G_i, H_i in (7)–(9) are given by

$$F_i(\xi,\eta,\rho)=f_i(\xi,\eta,\rho)-\sum_{j=1}^{r}N_j(\xi,\eta,\rho)f_{ij},\quad(10)$$

$$G_i(\xi,\eta,\rho)=g_i(\xi,\eta,\rho)-\sum_{j=1}^{r}N_j(\xi,\eta,\rho)g_{ij},\quad(11)$$

$$H_i(\xi,\eta,\rho)=h_i(\xi,\eta,\rho)-\sum_{j=1}^{r}N_j(\xi,\eta,\rho)h_{ij}.\quad(12)$$

In (10)–(12) f_i, g_i, h_i $(i=1,2,3)$ contain the asymptotic displacement functions that are coefficients of the mode-I, -II and -III stress intensity factors transformed to the global coordinate system. The terms f_{1j}, g_{1j}, h_{1j}, f_{2j}, g_{2j}, h_{2j}, f_{3j}, g_{3j}, h_{3j} in (10)–(12) are simply constants computed from the f_i, g_i, h_i functions evaluated at the jth node in the element. Hartranft and Sih (1969) showed that the crack tip fields along a 3D crack front in homogeneous materials are the same as those for a two-dimensional crack under plane strain conditions. Also, as mentioned previously, for two-dimensional cracks in FGMs, Delale and Erdogan (1983) and Eischen (1987) showed that the leading terms in the asymptotic local crack tip fields are the same as those for a corresponding homogeneous-isotropic material. Therefore, the local crack tip displacements for a 3D crack in an isotropic-homogeneous material can be used for cracks in FGMs by taking into account the spatial material property variation. These displacements are given by

$$\bar{u}=K_{\mathrm{I}}\bar{f}_1+K_{\mathrm{II}}\bar{g}_1,\quad \bar{v}=K_{\mathrm{I}}\bar{f}_2+K_{\mathrm{II}}\bar{g}_2,\quad \bar{w}=K_{\mathrm{III}}\bar{h},\quad(13)$$

where

$$\bar{f}_1 = \frac{1}{2E}\sqrt{\frac{r}{2\pi}}\left((5-3v-8v^2)\cos\left(\frac{\theta}{2}\right)-(1+v)\cos\left(\frac{3\theta}{2}\right)\right), \tag{14}$$

$$\bar{g}_1 = \frac{1}{2E}\sqrt{\frac{r}{2\pi}}\left((9+v-8v^2)\sin\left(\frac{\theta}{2}\right)+(1+v)\sin\left(\frac{3\theta}{2}\right)\right), \tag{15}$$

$$\bar{f}_2 = \frac{1}{2E}\sqrt{\frac{r}{2\pi}}\left((7-v-8v^2)\sin\left(\frac{\theta}{2}\right)-(1+v)\sin\left(\frac{3\theta}{2}\right)\right), \tag{16}$$

$$\bar{g}_2 = -\frac{1}{2E}\sqrt{\frac{r}{2\pi}}\left((3-5v-8v^2)\cos\left(\frac{\theta}{2}\right)+(1+v)\cos\left(\frac{3\theta}{2}\right)\right), \tag{17}$$

$$\bar{h} = \frac{2}{E}\sqrt{\frac{2r}{\pi}}(1+v)\sin\left(\frac{\theta}{2}\right). \tag{18}$$

In (13)–(18), E and v are the elastic constants evaluated at an arbitrary location in the vicinity of the crack tip based on material gradation. r and θ are measured locally from the crack front as shown in Fig. 2 for integration point A. A_0 is the intersection point on the crack front corresponding to integration point A. The relationship between the local crack tip displacement components $\bar{u}_i$, (13)–(18), and the global displacements u_i are found through the usual vector transformations. Using index notation

$$u_i = a_{ji}\bar{u}_j, \tag{19}$$

where a_{ji} represents the direction cosines between the primed axes and the global axes in Fig. 2, i.e., $a_{11} = \cos(x', x)$, $a_{12} = \cos(x', y)$, $a_{13} = \cos(x', z)$, etc. Transforming the asymptotic displacements in (13)–(18) to global coordinates yields the following terms for f_i,g_i, and h_i in (10)–(12)

$$f_i = \bar{f}_1 a_{1i} + \bar{f}_2 a_{2i}, \tag{20}$$

$$g_i = \bar{g}_1 a_{1i} + \bar{g}_2 a_{2i}, \tag{21}$$

$$h_i = \bar{h} a_{3i}. \tag{22}$$

It should be noted that, for a general three-dimensional problem, the direction cosines used to perform the local-to-global transformations are in general different at every point in the enriched element. In addition, for element coordinate values of ξ, η, ρ located at the element nodes, the displacements are simply given by the leading terms in Eqs. (7)–(9), since F_i, G_i, and H_i, (10)–(12), are identically zero at these points.

For the cases studied in this paper, where the crack is located in a graded material, the elastic modulus and Poisson's ratio in (14)–(18) can be functions of position and are evaluated accordingly for all integration and nodal points during the formation of element stiffness matrices and force vectors of enriched elements. Further specific details on integration of enriched element matrix and load vector can be found in Ayhan (1999).

3. Numerical examples

In this section, examples are provided that demonstrate the application of enriched finite elements to FGMs containing different types of three-dimensional cracks. The finite-element models presented in this paper are generated by using ANSYS™ and converted into FRAC3D model format. First, using solutions from the literature, comparisons are made in terms of stresses for a semi-infinite strip under different loads. Then, fracture solutions are obtained for different crack types using three-dimensional enriched elements and results are compared to available solutions in the literature. These include edge cracks in a semi-infinite strip with plane strain boundary conditions and two types of surface cracks, i.e., two different ellipticity ratios, contained in a finite-thickness plate. These applications serve as examples for validation of the method. Further analyses are also performed to study the free-surface effects on the fracture solution near the zone in which the crack front terminates.

3.1. Stresses in a functionally graded strip

Consider the semi-infinite strip shown in Fig. 1. As can be seen from this figure, three types of loads have been considered. These are uniform tensile load, bending and thermal load having temperature gradient in the

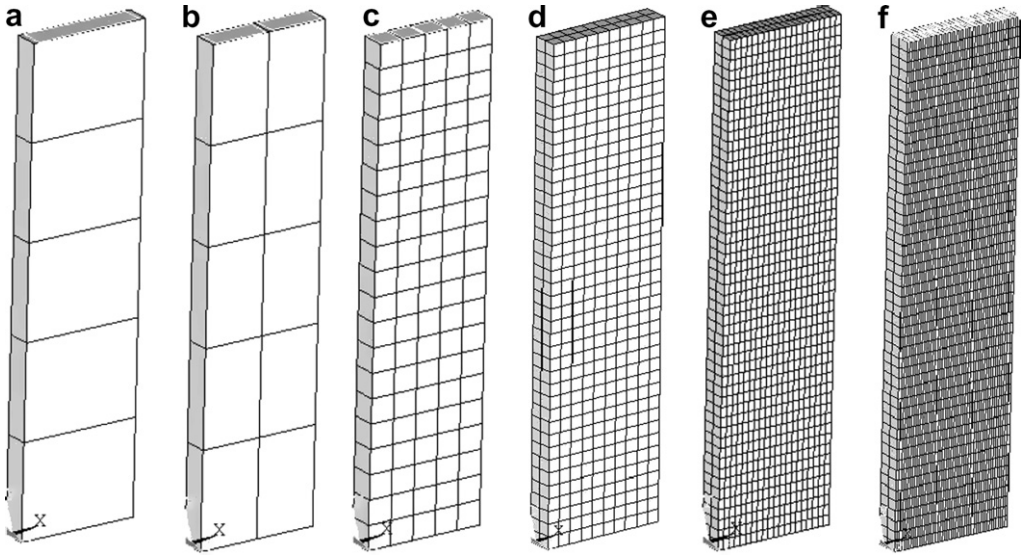

Fig. 3. Finite-element models of functionally graded strip: (a) 1 element, (b) 2 elements (c) 5 elements, (d) 10 elements, (e) 20 elements and (f) 50 elements in thickness direction.

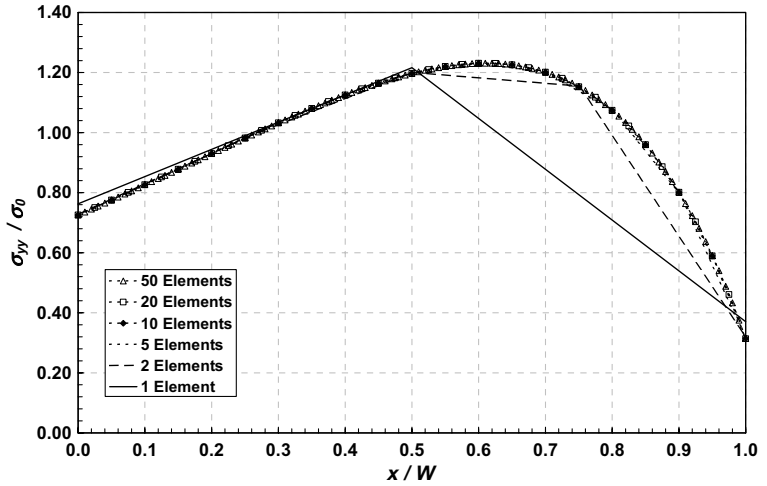

Fig. 4. Normalized σ_{yy} stresses for different levels of mesh refinement in thickness direction of the semi-infinite strip under uniform far-field tensile load – uncracked model.

material gradation direction. First, using the uniform tensile loading case ($E_2/E_1 = 10$), a mesh refinement study is performed. The results presented are nodal stresses that are extrapolated from the stresses at the integration points using the method described in Ayhan (1999).

Fig. 3 shows finite-element models having different number of elements in the direction of material gradation, ranging from 1 to 50 elements. As can be seen from these models, number of elements in the height and thickness directions is also changed to keep the elements at reasonable aspect ratios. Fig. 4 shows the normalized σ_{yy} stresses at the symmetry line, i.e., $y = 0$ in Fig. 1, for different levels of mesh refinement in the width direction for the case of uniform tensile load with plane strain conditions. The plane strain condition is achieved by prescribing zero out-of-plane displacements for all nodes in the model. The results are normalized based on the applied uniform far-field stress. As can be seen from this figure, the 5-element model is able to provide relatively continuous and accurate stress distribution when compared to the theoretical solution of

Erdogan and Wu (1997). It can also be seen that the 2-element model is able to capture the correct stresses at the nodal points as well, but is not discretized enough to capture the complete stresses distribution along the symmetry line. Furthermore, the 10-, 20- and 50-element models provide even a smoother representation of the analytical solution. Thus, in the following examples, 10 elements are used in the thickness direction.

In Fig. 5, normalized σ_{yy} stresses are plotted when the strip model is exposed to linear temperature gradient across the width W, $T_2 = 0.05T_0$ and $T_1 = 0.5T_0$. As in the study of Walters et al. (2004) the gradation in material properties follow the exponential form defined in (1) and are given as $E_2/E_1 = 10$ and $\alpha_2/\alpha_1 = 2$. Similar to the case of uniaxial loading, analyses are performed for cases with different number of elements across the width of the model. The normalization is done using

$$\sigma_n = E_1\alpha_1 T_0/(1-\nu). \tag{23}$$

It is seen from this figure that a minimum of 5–10 elements are needed to adequately represent the stress distribution across the width of the graded strip. When compared, it can be seen that the results agree well with those of Walters et al. (2004). It should be noted that these conclusions for mesh refinement can change for other gradation cases depending on the form and severity of the material property gradient, i.e., more or less elements may be needed for other material gradation cases.

Using 10 elements across the width of the strip model, the same thermal stress problem is also analyzed using quadratic 15-noded triangular prism and 10-noded tetrahedral elements shown in Fig. 6. Fig. 7 shows the finite-element meshes used. Fig. 8 shows that the normalized σ_{yy} stresses for triangular prism and tetrahedral mesh models are the same as those obtained from the all-hexahedral element model. As will be seen in the

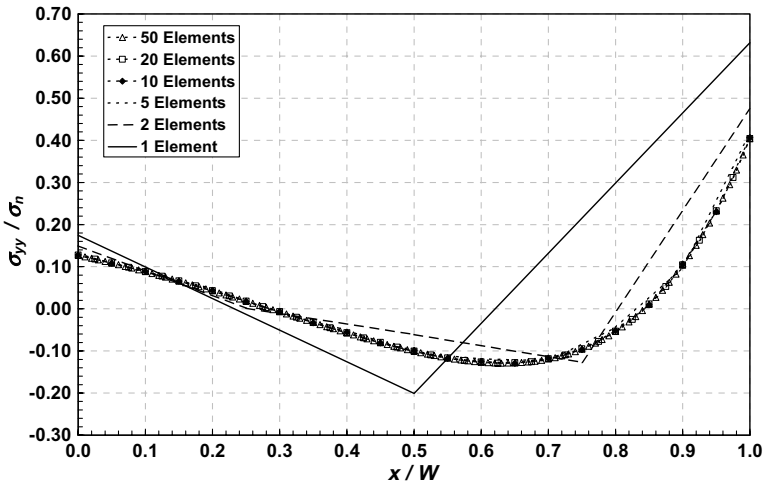

Fig. 5. Normalized σ_{yy} stresses for different levels of mesh refinement in thickness direction of the semi-infinite strip with linear temperature gradient – uncracked model.

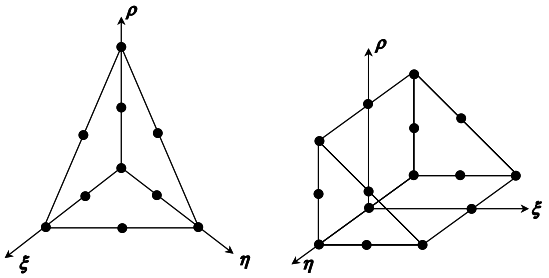

Fig. 6. 10-Node tetrahedral and 15-node triangular prism isoparametric finite elements.

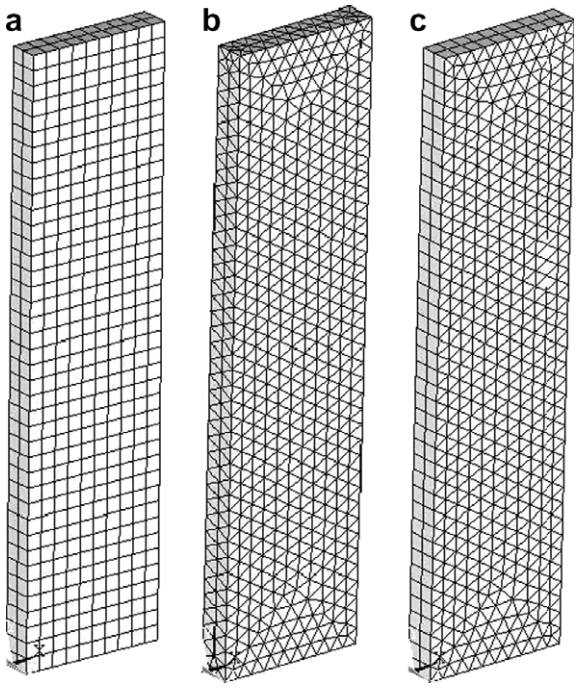

Fig. 7. Finite-element models. (a) 20-Node hexahedral elements, (b) 10-node tetrahedral elements and (c) 15-node triangular-prism elements.

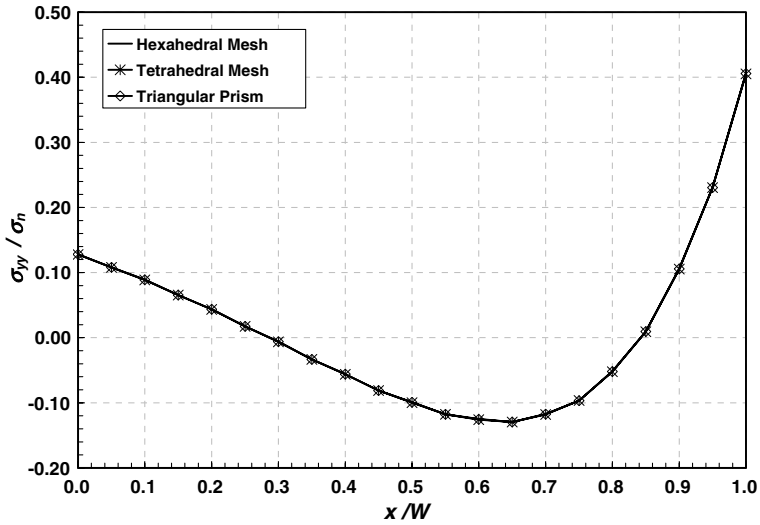

Fig. 8. Normalized σ_{yy} stresses on the uncracked semi-infinite strip with linear temperature gradient – comparison using different element types.

three-dimensional fracture models, mixed finite-element meshes are used that contain both tetrahedral and hexahedral quadratic elements. It is noted that in all of the cases presented in this paper, the material gradation effects are taken into account at the level of integration points, i.e., Gaussian integration points within an element have different material property values.

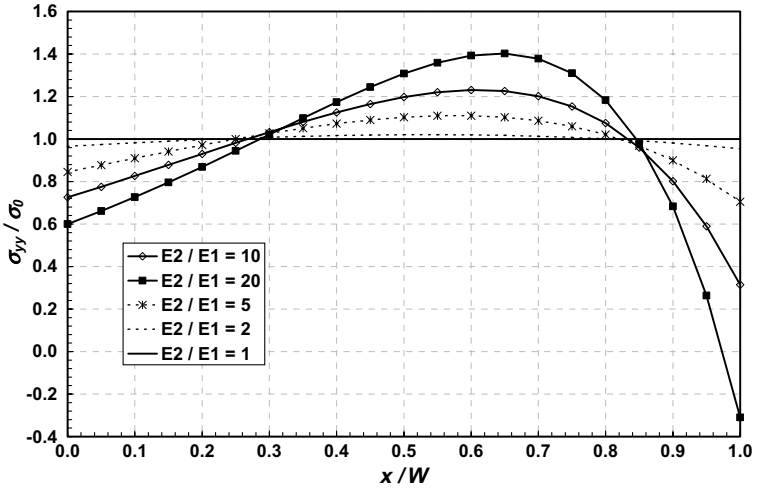

Fig. 9. Normalized σ_{yy} stresses for different levels of material gradation – uniform tensile far-field stress, uncracked model.

To demonstrate the accuracy of stresses for other material gradation cases, using the 10-element model, different E_2/E_1 ratios are considered for uniform tensile loading case and the normalized stresses are plotted in Fig. 9. These results also agree well with those of Erdogan and Wu (1997).

3.2. Fracture analysis of edge cracks in a functionally graded strip

This section includes results from fracture analyses of edge cracks in a functionally graded strip. The edge crack of length "a" is contained in a functionally graded semi-infinite strip shown in Fig. 1. As in the case of stress analysis of uncracked strip, the same form of material property gradation is considered, i.e., Eq. (1). First, a mesh refinement study is performed to identify the crack tip element size needed for converged and accurate stress intensity factors as compared to the solution of Erdogan and Wu (1997). Having determined the required element size, further analyses are performed to include uniform tensile far field and bending loads and different crack lengths. Fig. 10 shows the finite-element mesh details for $a/W = 0.5$. Note that due to symmetry with respect to "x" axis, only half of the geometry is modeled in the "y" direction. Also, in all of the edge crack solutions presented in this section, height of the symmetric FGM strip model is considered to be $10W$.

Considering a crack length $a/W = 0.7$, tensile uniform far-field loading and $E_2/E_1 = 10$, crack tip mesh refinement studies are performed. As a mesh refinement parameter, ratio of crack length and crack tip element size in the direction of material gradation, or equivalently parallel to the crack faces, is used.

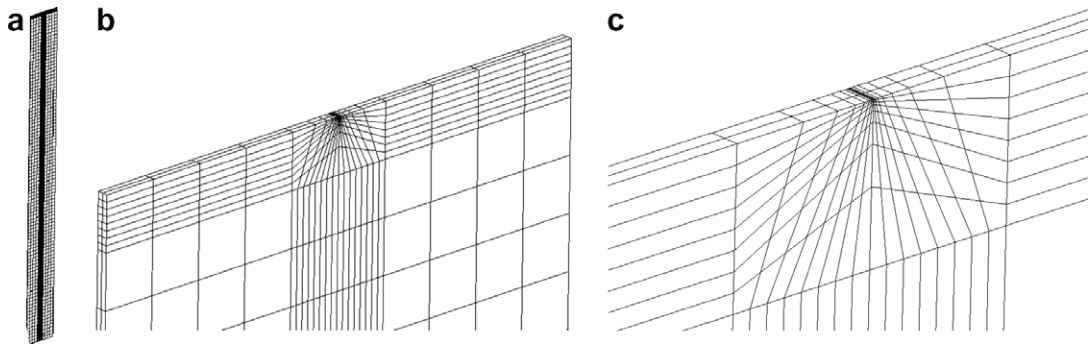

Fig. 10. Finite element model of a functionally graded strip containing an edge crack – a/W = 0.5 with crack tip element size $a/S_{tip} = 0.001$. (a) Global view, (b) close-up view of symmetry cross-section and (c) close-up view of crack tip region.

$$S_{\text{tip\_ref}} = a/S_{\text{tip}}. \tag{24}$$

Table 1 lists the normalized mode-I stress intensity factors for different levels of mesh refinement at the crack tip. The results are normalized by $K_R = \sigma_0(\pi a)^{0.5}$ and are included with and without linear transition elements. As can be seen from Table 1, cases with $S_{\text{tip\_ref}} > 300$ provide results that are within <1% agreement with the solution of Erdogan and Wu (1997). It is also worth noting that in the absence of transition elements, the percent difference changes its sign from negative to positive and keeps increasing with increased mesh refinement, whereas when the transition elements are included, the magnitude of difference keeps decreasing as the element size becomes smaller. This can clearly be seen in the % difference plot in Fig. 11. Thus, in the following studies, the element size at the crack tip is kept such that $S_{\text{tip\_ref}} \approx 1000$.

Using a mesh size at the crack tip with $S_{\text{tip\_ref}} = 1000$, enriched finite-element solutions are generated for the edge-cracked strip above for different crack lengths and functional gradient exponents. Tensile and bending loads are considered and results are compared to those of Erdogan and Wu (1997). Table 2 lists the normalized mode-I stress intensity factors and their comparison to Erdogan and Wu's (1997) solution for $E_2/E_1 = 5$ and $E_2/E_1 = 0.2$ with far-field uniform tensile load acting on the strip. As can be seen from this table, good agreement is obtained between the results of FRAC3D and the solution of Erdogan and Wu (1997). The maximum error occurs for $E_2/E_1 = 0.2$, $a/W = 0.7$ and is −3.2%. For all other cases, the error is less than or equal to 1.0%. Table 3 includes the above comparison for the case of bending load acting at the ends of the finite with strip shown in Fig. 1. The results are normalized by $K_R = \sigma_b(\pi a)^{0.5}$ where σ_b is the bending stress. Similar to the case of uniform tensile loading, all the results are within 1.0% agreement compared to those of Erdogan

Table 1
Normalized mode-I stress intensity factors, K_I/K_R, for an edge crack in an FGM strip – different mesh refinements at the crack tip and comparison with solution of Erdogan and Wu (1997)

$a/W = 0.7$	Erdogan and Wu (1997) – $K_I/K_R = 5.2865$			
	FRAC3D – K_I/K_R		% Difference	
S_tip/a	Transition	No transition	Transition	No transition
0.017000	4.8572	5.1250	−8.12	−3.06
0.009300	5.1332	5.2848	−2.90	−0.03
0.003100	5.2376	5.3387	−0.93	0.99
0.000721	5.2720	5.3519	−0.27	1.24

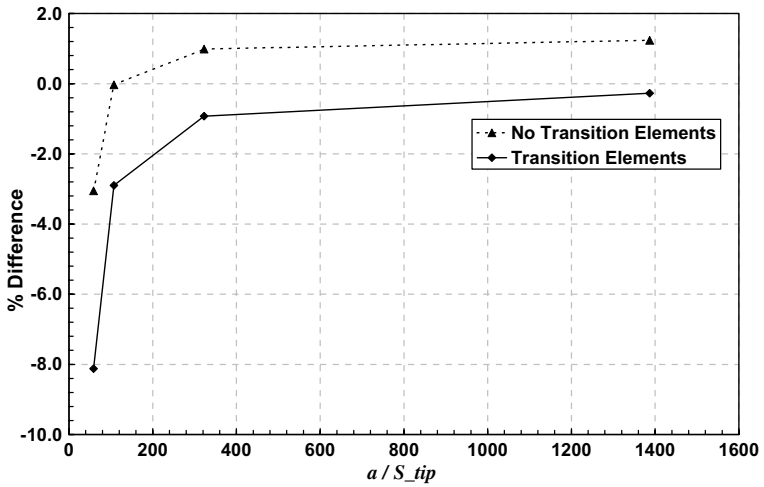

Fig. 11. % Difference vs. crack tip element size parameter for an edge crack in functionally graded strip as compared to solution of Erdogan and Wu (1997).

Table 2
Normalized mode-I stress intensity factors, K_I/K_R, for different crack sizes and material properties including comparison with solution of Erdogan and Wu (1997) – uniform tensile loading

a/W	$E_2/E_1 = 5$, $\beta = 1.609$			$E_2/E_1 = 0.2$, $\beta = -1.609$		
	Erdogan and Wu (1997)	FRAC3D	% Difference	Erdogan and Wu (1997)	FRAC3D	% Difference
0.1	0.9908	1.0003	1.0	1.0553	1.0600	0.4
0.2	1.1318	1.1400	0.7	1.3956	1.4036	0.6
0.3	1.3697	1.3786	0.6	1.8395	1.8513	0.6
0.4	1.7483	1.7572	0.5	2.4436	2.4541	0.4
0.5	2.3656	2.3757	0.4	3.3266	3.3267	0.0
0.6	3.4454	3.4581	0.4	4.7614	4.7266	−0.7
0.7	5.5830	5.5986	0.3	7.5248	7.2831	−3.2
0.8	10.8775	10.9121	0.3			

Table 3
Normalized mode-I stress intensity factors, K_I/K_R, for different crack sizes and material properties including comparison with solution of Erdogan and Wu (1997) – bending load

a/W	$E_2/E_1 = 5$, $\beta = 1.609$			$E_2/E_1 = 0.2$, $\beta = -1.609$		
	Erdogan and Wu (1997)	FRAC3D	% Difference	Erdogan and Wu (1997)	FRAC3D	% Difference
0.1	0.6385	0.6447	1.0	1.6743	1.6801	0.3
0.2	0.6871	0.6921	0.7	1.5952	1.6020	0.4
0.3	0.7778	0.7829	0.7	1.6122	1.6195	0.5
0.4	0.9236	0.9284	0.5	1.7210	1.7236	0.2
0.5	1.1512	1.1631	1.0	1.9534	1.9454	−0.4
0.6	1.5597	1.5654	0.4	2.4037	2.3711	−1.4
0.7	2.3360	2.3424	0.3	3.3536	3.2114	−4.2
0.8	4.2109	4.2245	0.3			

and Wu (1997), except for $a/W = 0.6$ and 0.7 with $E_2/E_1 = 0.2$. The results for these two cases differ from the solution of Erdogan and Wu (1997) by −1.4% and −4.2%, respectively.

3.3. Fracture analysis of surface cracks in finite-thickness FGM plates

Having demonstrated the accuracy of three-dimensional enriched elements as applied to two-dimensional edge crack problem in an FGM strip, three-dimensional surface crack problems are also considered. Fig. 12

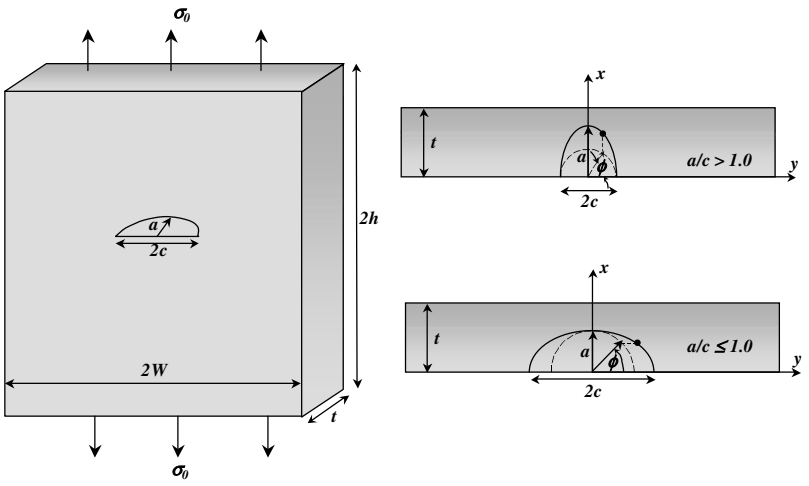

Fig. 12. Finite-thickness FGM plate containing a semi-elliptical surface crack under uniform tension loading.

shows such a semi-elliptical surface crack contained in an FGM plate. As can be seen in this figure, the material gradient is in the x-direction and the plate is under uniform far-field tensile load. Two cases of surface cracks are analyzed: (i) $a/t = 0.5$, $a/c = 2$, $E(t)/E(0) = 5$, $v = 0.25$; (ii) $a/t = 0.8$, $a/c = 1/3$, $E(t)/E(0) = 0.2$, $v = 0.25$. In these examples, the corresponding homogeneous cases are also studied and compared to the fracture solutions of the FGM plate.

Figs. 13 and 14 show the finite-element mesh details for the two crack geometries analyzed. As can be seen from these figures, only 1/4th of the plate is modeled to take advantage of the symmetry in y and z directions. The finite-element meshes are generated using 10-noded tetrahedral elements and contain 20-noded hexahedrons near the crack front. Along the crack front, 161 nodes, 80 quadratic elements and 201 nodes, 100

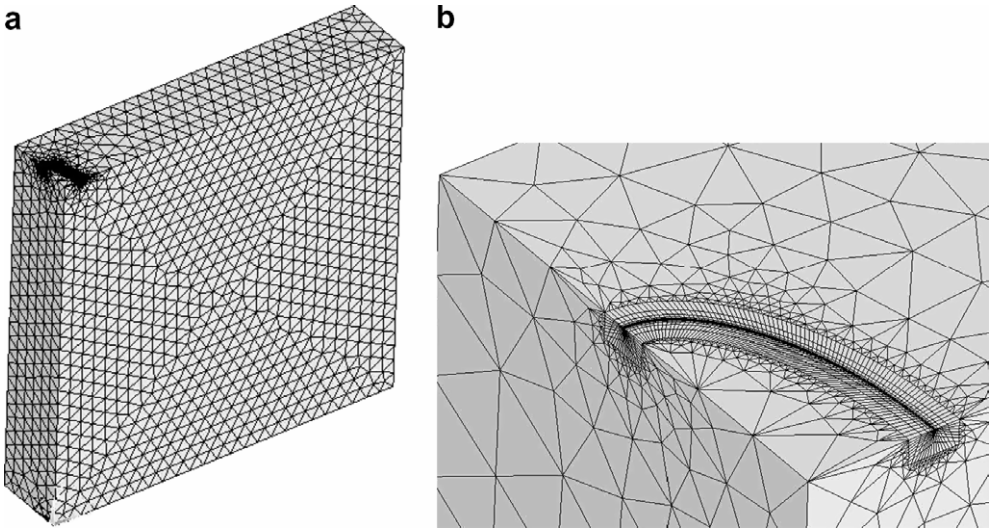

Fig. 13. Finite-element model of FGM plate containing semi-elliptical surface crack, $a/t = 0.5$, $a/c = 2$. (a) Overall view and (b) close-up view of the crack region.

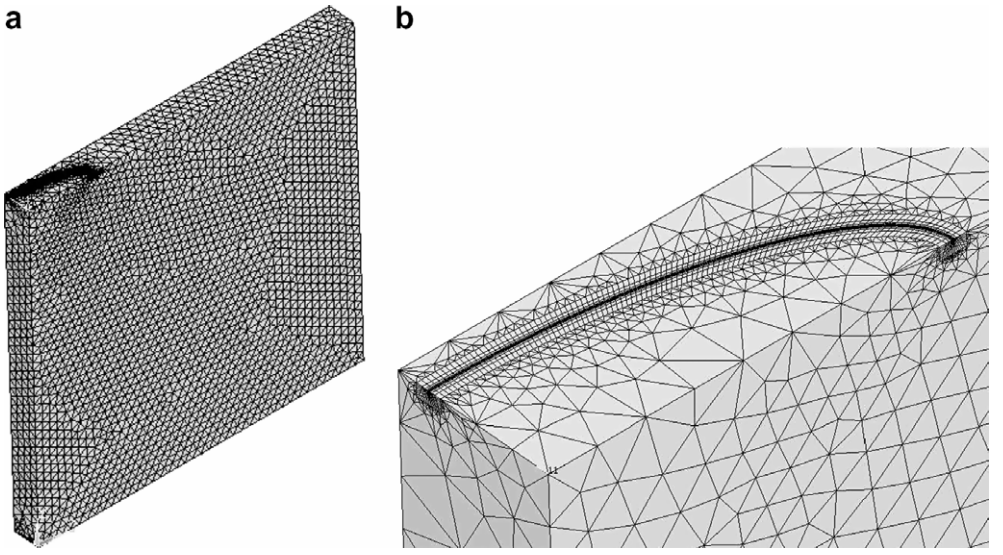

Fig. 14. Finite-element model of FGM plate containing semi-elliptical surface crack, $a/t = 0.8$, $a/c = 1/3$. (a) Overall view and (b) close-up view of the crack region.

quadratic elements are used for cracks in Figs. 13 and 14, respectively. These models have 52,861 quadratic elements – 106,357 nodes, and 77,817 quadratic elements – 143,350 nodes, respectively.

Fig. 15 shows the comparison of the enriched element solution to the results of Walters et al. (2004) and Yildirim et al. (2005) for the same problem with $a/t = 0.5$ and $a/c = 2$. As can be seen from this figure, good agreement is obtained between the different solutions for both homogeneous and FGM cases. The stress intensity factor is normalized by

$$K_R = \sigma_0 \sqrt{\frac{\pi a}{Q}}. \tag{25}$$

The shape factor, Q, denotes the square of the complete elliptic integral of the second kind and $\sqrt{Q}$ equals half the arc length of an ellipse divided by the length of the major axis (Walters et al., 2004). Q is commonly approximated by

$$Q = \begin{cases} 1 + 1.464(a/c)^{1.65} & \text{if } (a/c) \leqslant 1, \\ 1 + 1.464(c/a)^{1.65} & \text{if } (a/c) > 1. \end{cases} \tag{26}$$

The definition of the crack front position parametric angle is shown in Fig. 12. Considering the same problem and by changing the crack tip element sizes in the tangential and perpendicular (*S_tip*) directions to the crack front, a mesh convergence study is also performed. Table 4 lists the finite-element model information on different models used for both $a/c = 2$ and $a/c = 0.33$, and Fig. 16 shows the comparison of normalized mode-I stress intensity factors along the crack front ($a/c = 2$). It can be seen from Fig. 16 that the results from the model with $S_{\text{tip\_ref}} = 250$ agree well with those of $S_{\text{tip\_ref}} = 1000$. Also, the number of elements and nodes from the coarse model ($S_{\text{tip\_ref}} = 250$) are comparable to those of Yildirim et al. (2005), who employed the

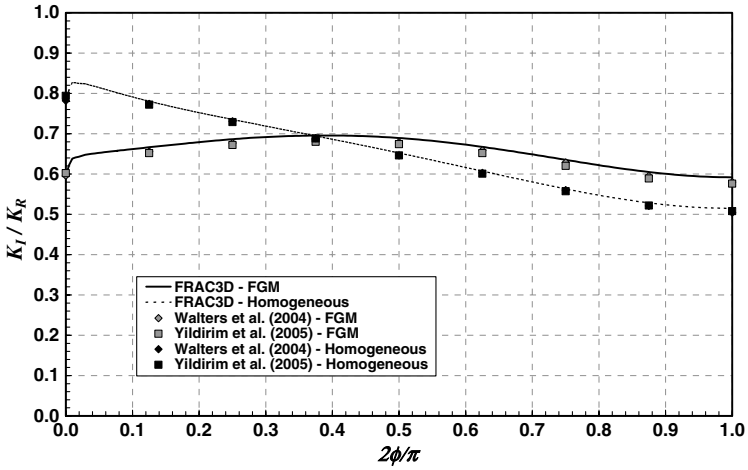

Fig. 15. Normalized mode-I stress intensity factors and comparison with other solutions, $a/t = 0.5$, $a/c = 2$, $v = 0.25$, $E(t)/E(0) = 5$ and homogeneous material.

Table 4
Finite-element model information for surface crack mesh sensitivity analysis

a/S_tip	$a/c = 2$			$a/c = 0.33$		
	Crack elements	Elements	Nodes	Crack elements	Elements	Nodes
1000	80	52,861	106,357	100	77,817	143,350
500	50	39,012	71,814	70	34,946	67,768
250	40	11,899	26,597	50	27,958	50,554

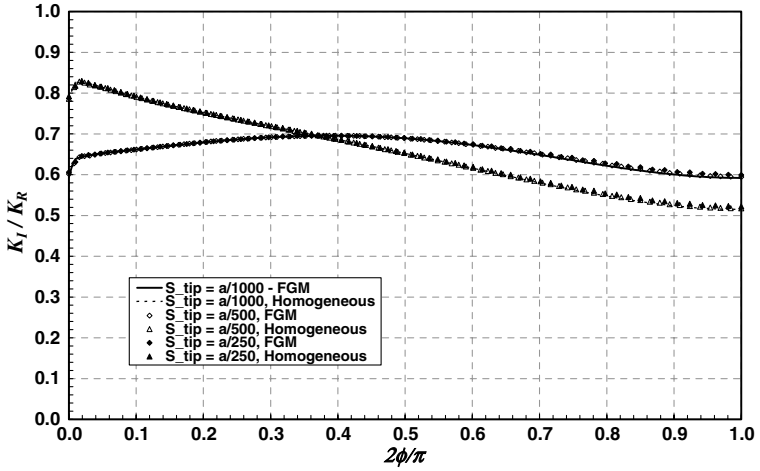

Fig. 16. Normalized mode-I stress intensity factors for crack tip mesh refinement study, $a/t = 0.5$, $a/c = 2$, $v = 0.25$, $E(t)/E(0) = 5$ and homogeneous material.

displacement correlation technique (DCT) combined with direct finite-element simulation to compute the stress intensity factor.

Fig. 17 shows the comparison of normalized mode-I stress intensity factors for homogeneous and FGM cases for a surface crack with $a/c = 0.33$ and $a/t = 0.8$ under uniform tension loading (Fig. 14). The FGM in this case had $E(t)/E(0) = 0.2$ and $v = 0.25$. It can be seen from this figure also that the results of enriched element agree well with those of Walters et al. (2004) and Yildirim et al. (2005) everywhere along the crack front except the free-surface region, where there is nearly 7% difference with respect to the solution of Walters et al. (2004). In the next section, more detailed results are presented for the behavior of stress intensity factor near the free surface. Similar to the case of $a/c = 2$, Fig. 18 shows the normalized mode-I stress intensity factors for different levels of mesh refinement listed in Table 4 ($a/c = 0.33$). Again, good level of agreement is obtained between solutions from the coarsest ($S_{\text{tip\_ref}} = 250$) and the finest ($S_{\text{tip\_ref}} = 1000$) models.

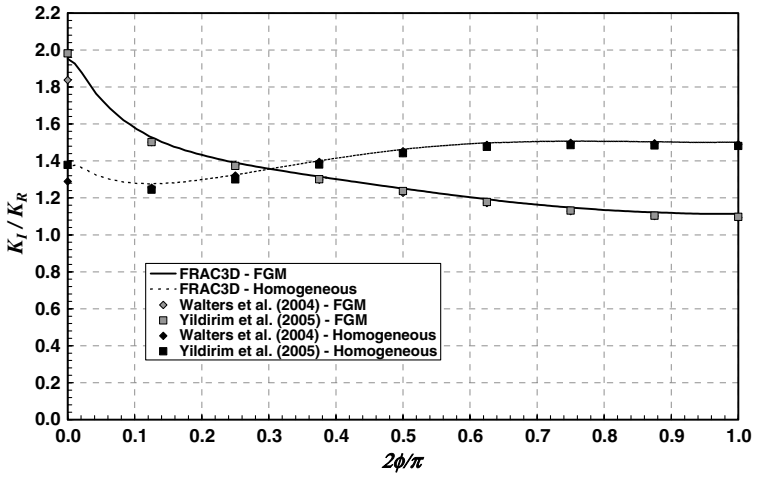

Fig. 17. Normalized mode-I stress intensity factors and comparison with other solutions, $a/t = 0.8$, $a/c = 1/3$, $v = 0.25$, $E(t)/E(0) = 0.2$ and homogeneous material.

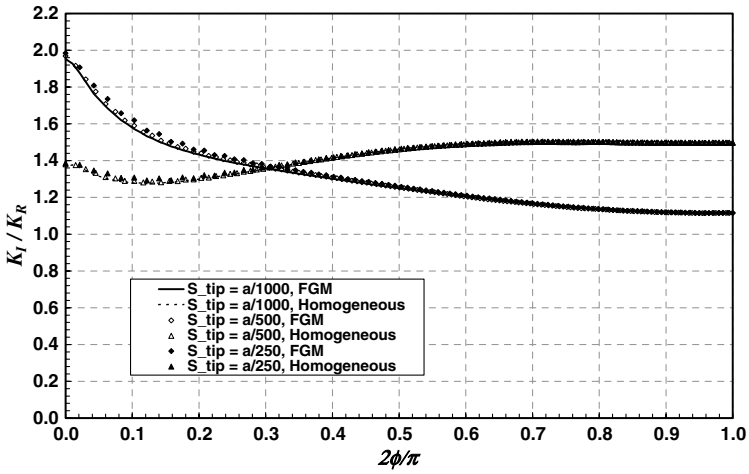

Fig. 18. Normalized mode-I stress intensity factors for crack tip mesh refinement study, $a/t = 0.8$, $a/c = 1/3$, $\nu = 0.25$, $E(t)/E(0) = 0.2$ and homogeneous material.

3.4. Stress intensity factors near free surface

It is well known that for three-dimensional cracks, there is a free-surface or boundary layer effect on the stress intensity factors. Benthem (1977) and Bazant and Estenssoro (1979) are among those who initially studied this phenomenon concluding that the stress singularities at the free surface are a function of the angle of intersection between crack front and free surface and the Poisson's ratio, ν. For a 90° crack/free-surface intersection ($\nu = 0.3$), the singular term associated with mode-I behavior is weaker than $r^{-1/2}$ and for mode-II and -III conditions, the singular terms are stronger than $r^{-1/2}$. Thus, using the conventional definition for the stress intensity factor means that at the free surface $K_I = 0$ and $K_{II} = K_{III} = \infty$. As stated by Joseph and Erdogan (1989), if a process such as the sub-critical crack growth requires that the strength of the stress singularity, i.e., stress intensity factor based on the square root singularity, be the primary driving force, then it is reasonable to expect that the power of stress singularity would be the same along the entire propagating front of the crack, including the free-surface region. This, in turn, would imply that if the Poisson's ratio is greater than zero, the intersection angle, measured from within the cracked surface, would need to be greater than 90° for mode-I loading and less than 90° for mode-II and -III loading.

In this section, the detailed behavior of mode-I stress intensity factors near the free surface for three-dimensional cracks in FGMs is studied. The crack front finite-element mesh for the above $a/c = 1/3$ surface crack problem (Fig. 14) is successively refined in this region along the crack front direction until a converged solution is obtained. Fig. 19 shows an example finite-element mesh near crack surface and the close-up view of the

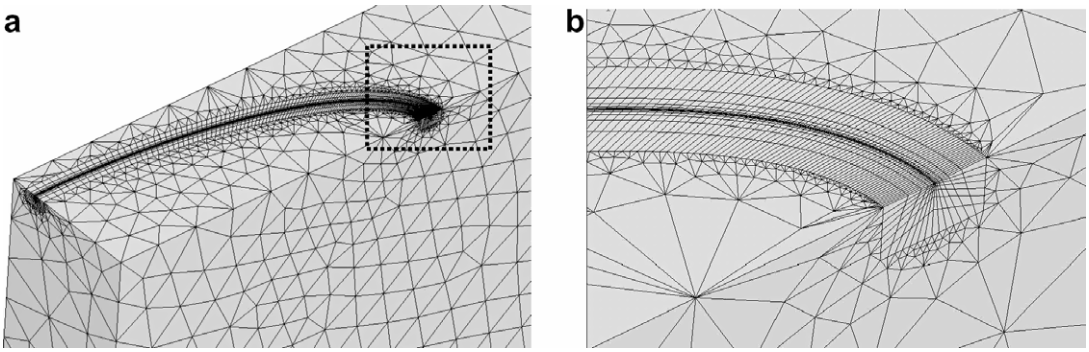

Fig. 19. Finite-element mesh for $a/c = 1/3$ with surface refinement. (a) Crack region and (b) free surface, "c", region.

free surface, "c", region. Note that the finite-element mesh refinement along the front direction is biased towards the "c" location. In the particular mesh shown in this figure, the thickness of the last element on the free-surface corresponds to $\phi = 0.41°$ in terms of parametric crack front position angle defined in Fig. 12. Fig. 20 shows results from different levels of surface mesh refinements and the baseline solution presented in Fig. 17. Fig. 20a–c show the detailed distributions of the normalized mode-I stress intensity factors along the whole front, in the first 0.03°, and 0.0025° segments, respectively. The angle values in the legends are the corresponding element thickness for the last element on the free surface in terms of the parametric position angle. It can be seen from Fig. 20b that the free-surface affects the stress intensity factors in the first 2% of the crack front as compared to the baseline solution without surface mesh refinement. It is also seen that the drop in stress intensity factors takes place near the first 0.5% of the crack front. Looking at the free-surface region more closely, Fig. 20c shows that the first two mesh refinement cases ($\phi_{\text{free}} = 0.0844°$ and $\phi_{\text{free}} = 0.0176°$) provide somewhat fluctuating results whereas the last two refinements ($\phi_{\text{free}} = 0.0033°$ and $\phi_{\text{free}} = 0.0008°$) provide a smooth and same distributions of the stress intensity factor in the immediate vicinity of the free surface. Therefore, a converged solution is obtained with respect to mesh size on the free surface. Although a considerable drop in the stress intensity factor is observed, it is still far from being zero at the surface location. As mentioned previously, in the enriched element method, the crack front nodal stress intensity factors are included as additional unknowns in the element formulation and are solved directly along with the nodal displacements. Therefore, this method allows prescribing stress intensity factor values to any nodal location on the crack front. Knowing that the mode-I stress intensity factor is zero at the free surface, for the refinement cases shown in Fig. 20, additional analyses are also performed with a "zero" stress intensity factor constraint at this location and the results are included in Fig. 21. Note that the solutions are the same, in the interior region of the crack front, as those without K constraint at the free surface. It is also observed that similar to Fig. 20, the first two refinement cases provide a non-smooth distribution of stress intensity factor near the free surface, whereas the last two cases provide stress intensity factor distributions that go to zero smoothly and are the same. Therefore, these two solutions ($\phi_{\text{free}} = 0.0033°$ and $\phi_{\text{free}} = 0.0008°$) are considered to be the "true" behavior of stress intensity factor distribution in the immediate vicinity of the free surface. It is also observed that the overall solution is not affected by the free-surface mesh refinement and K constraint effects anywhere on the crack front, except the immediate vicinity of the free-surface region (Figs. 20 and 21). The refinement cases shown in Figs. 20 and 21 had 361, 801, 801, and 801 nodes (180, 400, 400 and 400 quadratic elements) along the crack front, respectively. Different levels of free-surface element sizes are obtained by modifying the mesh biasing towards the free surface. Also, it was not possible to mesh the entire domain for the last two cases of refinement ($\phi_{\text{free}} = 0.0033°$ and $\phi_{\text{free}} = 0.0008°$) by keeping a reasonable element size everywhere on the model, and therefore a sub-modeling approach was taken. The solution from $\phi_{\text{free}} = 0.0176°$ (full model) is used to map the nodal displacements as boundary conditions onto the external surfaces of the hexahedral near-front mesh shown in Fig. 22. Having applied the interpolated boundary conditions and keeping the applicable symmetry boundary conditions along with FGM properties, the near-front hexahedral model is used for the finite-element solution including direct computation of stress intensity factors.

4. Summary and conclusions

Functionally graded materials (FGMs) have long been recognized for their numerous advantages. Extensive developments and studies have been performed to understand their materials characteristics and mechanical behavior in different engineering applications including fracture mechanics. In this study, a three-dimensional enriched finite-element methodology as applied to FGMs is presented. A general-purpose finite-element program, FRAC3D, is enhanced for this capability. It is shown that enriched finite elements allow accurate and efficient computation of fracture parameters, i.e., stress intensity factors, for elastic three-dimensional cracks in FGMs. First, comparisons are made to available solutions in the literature in terms of stresses in an FGM strip under different loads. The enriched element methodology is applied to mode-I edge-cracked FGM strip and surface-cracked FGM plate and the computed stress intensity factors provided good agreement with available solutions in the literature. It is also shown that the enriched elements are capable of capturing the detailed behavior of stress intensity factors near the free surface by allowing

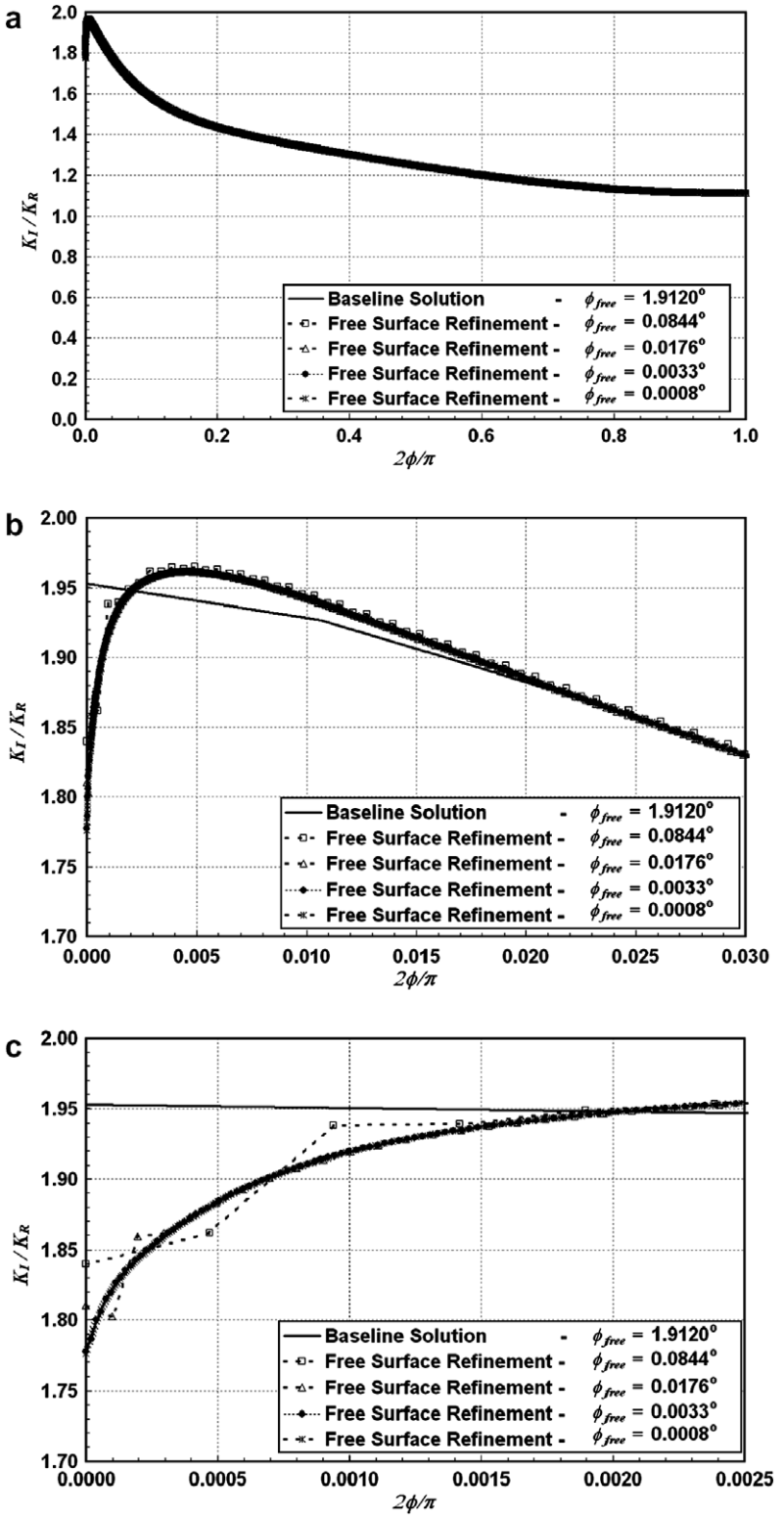

Fig. 20. Mode-I stress intensity factor distribution for different ranges of crack front position – no free-surface constraint on K_I.

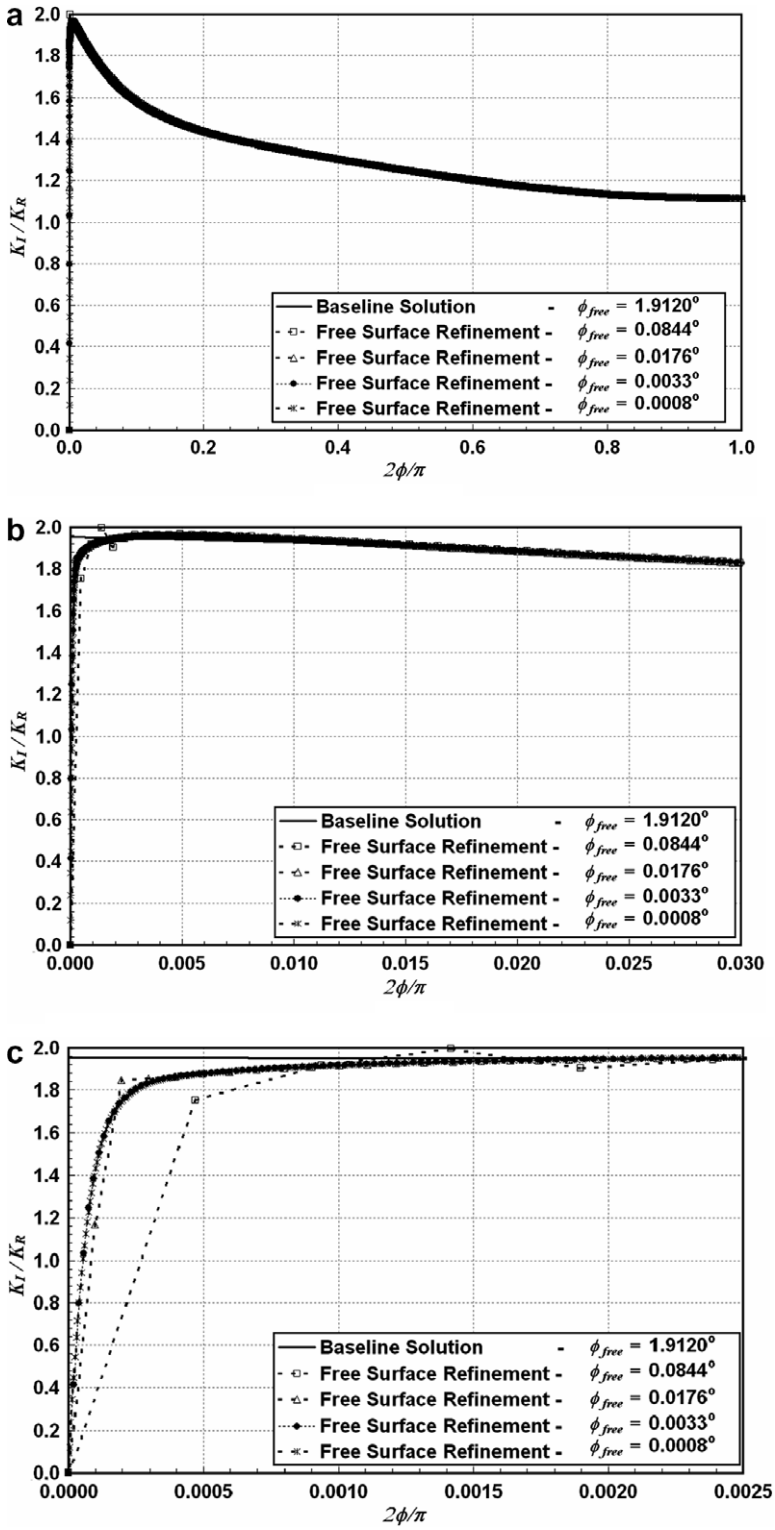

Fig. 21. Mode-I stress intensity factor distribution for different ranges of crack front position – $K_I = 0$ at the free surface.

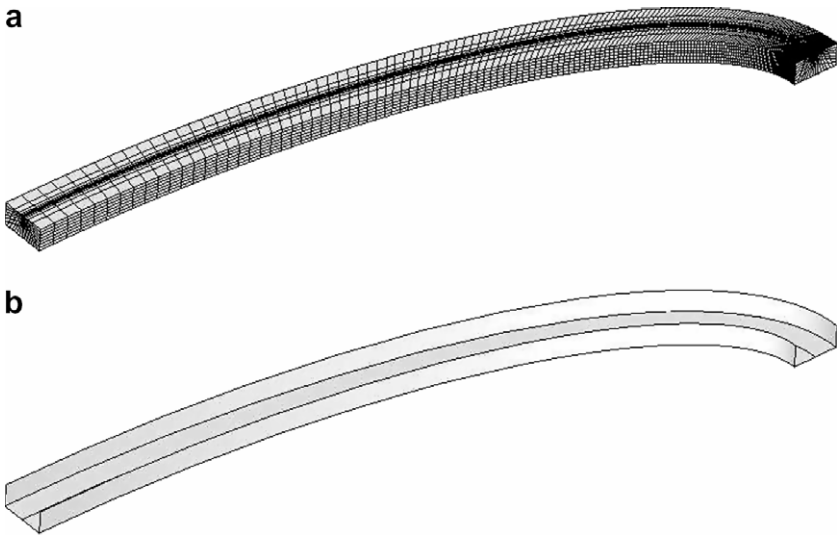

Fig. 22. Finite-element model used for sub-model, $a/c = 1/3$. (a) Finite-element mesh and (b) external surfaces where interpolated nodal displacements applied from the full model.

prescription of "zero" stress intensity factor at the free-surface node, which is located on the crack front termination point. It is concluded that the enriched elements can be applied to three-dimensional cracks in FGMs accurately and efficiently without the need of special meshes near the crack front and detailed post-processing of the finite-element solution.

References

Abanto-Bueno, J., Lambros, J., 2002. Investigation of crack growth in functionally graded materials using digital image correlation. Engineering Fracture Mechanics 69, 1695–1711.

Anlas, G., Lambros, J., Santare, M.H., 2002. Dominance of asymptotic crack tip fields in elastic functionally graded materials. International Journal of Fracture 115, 193–204.

ANSYS, 2004. Theory Manual Version 9.0. Ansys Inc., Canonsburg, PA, USA.

Ayhan, A.O., 1999. Finite element analysis of nonlinear deformation mechanisms in semiconductor packages. Ph.D. Dissertation, Lehigh University.

Ayhan, A.O., Nied, H.F., 1999. FRAC3D-finite element based software for 3-D and generalized plane strain fracture analysis (second revision). SRC Technical Report.

Ayhan, A.O., Nied, H.F., 2002. Stress intensity factors for three-dimensional surface cracks using enriched finite elements. International Journal for Numerical Methods in Engineering 54 (6), 899–921.

Ayhan, A.O., 2004. Mixed-mode stress intensity factors for deflected and inclined surface cracks in finite-thickness plates. Engineering Fracture Mechanics 71 (7–8), 1059–1079.

Ayhan, A.O., 2007. Mixed-mode stress intensity factors for deflected and inclined corner cracks in finite-thickness plates. International Journal of Fatigue 29 (2), 305–317.

Bazant, Z.P., Estenssoro, L.F., 1979. Surface singularity and crack propagation. International Journal of Solids and Structures 15, 405–426.

Benthem, J.P., 1977. State of stress at the vertex of a quarter-infinite crack in a half-space. International Journal of Solids and Structures 13, 479–492.

Butcher, R.J., Rousseau, C.E., Tippur, H.V., 1998. A functionally graded particulate composite: preparation, measurements and failure analysis. Acta Materialia 47 (1), 259–268.

Carpenter, R.D., Paulino, G.H., Munir, Z.A., Gibeling, J.C., 2000. A novel technique to generate sharp cracks in metallic/ceramic functionally graded materials by reverse 4-point bending. Scripta Materialia 43, 547–552.

Cook, R.D., Malkus, D.S., Plesha, M.E., 1989. Concepts and Applications of Finite Element Analysis. John Wiley & Sons.

Delale, F., Erdogan, F., 1983. The crack problem for a nonhomogeneous plane. Journal of Applied Mechanics 50, 609–614.

Dolbow, J.E., Gosz, M., 2002. On the computation of mixed-mode stress intensity factors in functionally graded materials. International Journal of Solids and Structures 39, 2557–2574.

Eischen, J.W., 1987. Fracture of nonhomogeneous materials. International Journal of Fracture 34, 3–22.

Erdogan, F., 1995. Fracture mechanics of functionally graded materials. Composites Engineering 5 (7), 753–770.

Erdogan, F., Wu, B.H., 1997. The surface crack problem for a plate with functionally graded properties. Journal of Applied Mechanics 64, 449–456.

Hartranft, R.J., Sih, G.C., 1969. The use of eigenfunction expansions in the general solution of three-dimensional crack problems. Journal of Mathematics and Mechanics 19, 123–138.

Joseph, P.F., Erdogan, E., 1989. Surface crack problems in plates. International Journal of Fracture 41, 105–131.

Konda, N., Erdogan, F., 1994. The mixed-mode crack problem in a nonhomogeneous elastic medium. Engineering Fracture Mechanics 47, 533–545.

Lee, Y.-D., Erdogan, F., 1995. Residual/thermal stresses in FGM and laminated thermal barrier coatings. International Journal of Fracture 69, 145–165.

Parameswaran, V., Shukla, A., 1998. Dynamic fracture of a functionally gradient material having discrete property variation. Journal of Material Science 33, 3303–3311.

Parameswaran, V., Shukla, A., 2002. Asymptotic stress fields for stationary cracks along the gradient in functionally graded materials. Journal of Applied Mechanics 69, 240–243.

Rice, J.R., 1968. A path-independent integral and the approximate analysis of strain concentration by notches and cracks. ASME Journal of Applied Mechanics 35, 379–386.

Walters, M.C., Paulino, G.H., Dodds, R.H., 2004. Stress-intensity factors for surface cracks in functionally graded materials under mode-I thermomechanical loading. International Journal of Solids and Structures 41, 1081–1118.

Walters, M.C., Paulino, G.H., Dodds, R.H., 2006. Computation of mixed-mode stress intensity factors for cracks in three-dimensional functionally graded solids. Journal of Engineering Mechanics 132, 1–15.

Williams, M.L., 1957. On the stress distribution at the base of a stationary crack. Journal of Applied Mechanics 24, 109–114.

Yildirim, B., Dag, S., Erdogan, F., 2005. Three dimensional fracture analysis of FGM coatings under thermomechanical loading. International Journal of Fracture 132, 369–395.